

# Electronic structure and unconventional non-linear response in double Weyl semimetal SrSi<sub>2</sub>

Banasree Sadhukhan<sup>1,2,\*</sup> and Tanay Nag<sup>3,†</sup>

<sup>1</sup>*KTH Royal Institute of Technology, AlbaNova University Center, SE-10691 Stockholm, Sweden*

<sup>2</sup>*Leibniz Institute for Solid State and Materials Research,  
IFW Dresden, Helmholtzstr. 20, 01069 Dresden, Germany*

<sup>3</sup>*Institut für Theorie der Statistischen Physik, RWTH Aachen University, 52056 Aachen, Germany*

(Dated: December 16, 2021)

Considering a non-centrosymmetric, non-magnetic double Weyl semimetal (WSM) SrSi<sub>2</sub>, we investigate the electron and hole pockets in bulk Fermi surface behavior that enables us to characterize the material as a type-I WSM. We study the structural handedness of the material and correlate it with the distinct surface Fermi surface at two opposite surfaces following an energy evolution. The Fermi arc singlet becomes doublet with the onset of spin orbit coupling that is in accordance with the topological charge of the Weyl Nodes (WNs). A finite energy separation between WNs of opposite chirality in SrSi<sub>2</sub> allows us to compute circular photogalvanic effect (CPGE). Followed by the three band formula, we show that CPGE is only quantized for Fermi level chosen in the vicinity of WN residing at higher value of energy. Surprisingly, for the other WN of opposite chirality in the lower value of energy, CPGE is not found to be quantized. Such a behavior of CPGE is in complete contrast to the time reversal breaking WSM where CPGE is quantized to two opposite plateau depending on the topological charge of the activated WN. We further analyze our finding by examining the momentum resolved CPGE. Finally we show that two band formula for CPGE is not able to capture the quantization that is apprehended by the three band formula.

## I. Introduction

The concept of chirality, determined by the fact whether an object is superimposable with its mirror image, is present in various research fields from biology to high energy physics. The chiral crystals have a well defined structural handedness due to the lack of inversion, mirror, or other roto-inversion symmetries. Such symmetry breaking manifest themselves through many fascinating properties e.g., optical activity [1], negative refraction [2], unusual superconductivity [3], quantized circular photogalvanic effect (CPGE) [4–7], gyrotropic magnetic effect [8], unusual phonon dynamics, chiral magnetoelectric effects [9, 10], magnetic Skyrmions [11] and many more. The structural handedness thus imprints its effect in topological responses for chiral semimetals. The fourfold degeneracy of the linear band touching in Dirac semimetals (DSMs) such as Cd<sub>3</sub>As<sub>2</sub> and Na<sub>3</sub>Bi, is broken by either time reversal or inversion symmetry leading to Weyl semimetals (WSMs) with isolated twofold non-trivial band crossings [12–14].

In this process, WSM is found to exhibit Weyl nodes (WNs), protected by a certain crystalline symmetries, that act as monopoles or anti-monopoles of Berry curvature in momentum space, with integer topological charge  $n$  [15–19]. On the other hand, DSMs have net vanishing topological charge  $n = 0$  [12–14]. As compared to the conventional WSMs with  $n = 1$  [20–22], the multi-WSMs have higher topological charge  $n > 1$  with the crystalline

symmetries bounding its maximum value to three [23–25]. The double-WSM (triple-WSM) show linear dispersion along one symmetry direction and quadratic (cubic) energy dispersion relations in remaining two directions respectively. We note that higher topological charge is also observed for multifold band crossing with integer spin in topological chiral crystals such as, the transition metal mono-silicides MSi ( $M = \text{Co, Mn, Fe, Rh}$ ) [26–30]. The Fermi arc surface states and chiral anomaly induced negative magnetoresistance directly reflect the topological nature of WSM through its transport signatures [31, 32].

Apart from first order electromagnetic and thermal responses [32–39], WSMs are further studied in the context of second order transport response namely, CPGE. The WSMs are found to exhibit quantized CPGE response where direction of DC photocurrent depends on the helicity of the absorbed circularly polarized photons [40–42]. The optical transitions near a WN plays an important role in quantization of CPGE serving as a direct experimental probe to measure the Chern numbers in topological WSMs [43, 44]. It is noteworthy that the breaking of inversion symmetry guarantees a finite CPGE. To be precise, the breaking of inversion symmetry (while preserving mirror symmetry) and tilting of the Weyl cones in non-centrosymmetric TaAs family cause a giant non-zero and non-quantized CPGE response [6, 45–51]. On the other hand, non-degenerate WNs can only result in a quantized CPGE referring to chiral nature of the underlying system where all mirror symmetries are broken [4, 8, 52]. More importantly, it has been shown considering a time reversal symmetry invariant WSM lattice model that quantization in CPGE is substantially different from a time reversal broken WSM [53].

\* banasree@kth.se

† tnag@physik.rwth-aachen.de

The double WSM state has been theoretically predicted recently in non-centrosymmetric  $\text{SrSi}_2$  that preserves time reversal symmetry [54, 55]. From the technological perspective, in general, non-centrosymmetric WSMs can be useful in designing the high-efficiency solar cells [45, 56]. A finite energy separation between two WNs with opposite topological charge makes  $\text{SrSi}_2$  an ideal material to study the CPGE. Hence a natural question arises that how does CPGE behave in such a non-magnetic double WSM. Our quest is indeed genuine due to the fact that  $\text{SrSi}_2$  is categorically different from TaAs WSM family as far as their electronic structures are concerned. At the same time, our study is equally relevant in the context of possible device application such as solar cell and experimental realizations.

In this work, we find  $\text{SrSi}_2$  has a structural handedness with enantiomeric properties. This is manifested in the surface Fermi surface (SFS) profile where Fermi arc exhibits inverted structure in two opposite surfaces (001) and (00 $\bar{1}$ ). The bulk Fermi surface, on the other hand, bears the information of electron and hole pocket referring to  $\text{SrSi}_2$  as a type-I WSM. We observe a quantized CPGE response in  $\text{SrSi}_2$  when Fermi level is kept in the vicinity of the WN at higher energy while there is no quantization for other WN at lower energy. Our finding is in accordance with the fact that CPGE behaves qualitatively distinct manner time reversal invariant WSM as compared to time reversal broken WSM [53]. We examine the evolution of CPGE with Fermi level considering spin orbit coupling (SOC) into the calculation and compare it to the bare calculation with generalized gradient approximation (GGA) only. Both the findings match qualitatively with each other while topological charge is found to be  $n = 2$  ( $n = 1$ ) followed by GGA+SOC (GGA) calculations. We anchor our findings with the momentum resolved analysis of CPGE. Furthermore, we check that two band formula for CPGE is unable predict the quantization that is correctly described by the three band formula. In short, our study uncovers various interesting non-linear optical response properties of  $\text{SrSi}_2$  besides its implications based on structural properties.

The organization of the paper is as follows. In Sec. II, we discuss the crystal structure, electronic band structure, position of the WNs and other other bulk properties (Fermi surface, Berry curvature). In Sec. III, we present the surface properties such as surface Fermi surface, spectral energy distribution and Fermi arcs, employing the slab geometry. We next describe the framework of CPGE and the associated results in Sec. IV. We provide the analysis on two band formula alongside there. We discuss the necessary computational details within the individual sections accordingly. Finally, in Sec. V, we end by the conclusion and outlook.

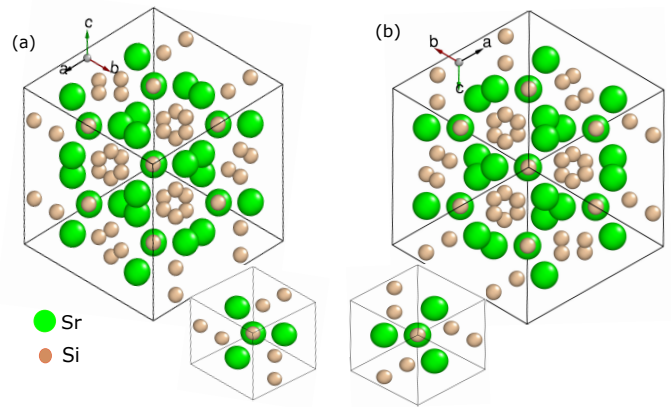


FIG. 1. (a) Crystal structure of  $\text{SrSi}_2$  showing the (111) view of two enantiomers for single (lower) and double (upper) the unit cell. (b) The crystal structure viewed from  $(\bar{1}\bar{1}\bar{1})$  which is the mirror ( $a \rightarrow b$ ,  $b \rightarrow a$  and  $c \rightarrow c$ ) + flipped image ( $a \rightarrow -b$ ,  $b \rightarrow -a$  and  $c \rightarrow -c$ ) of (a). Structural chirality generates a distinct handedness under a mirror operation referring to the enantiomeric property of the material.

## II. Topological characterization

$\text{SrSi}_2$ , crystallizing in a cubic Bravais lattice, has the chiral space group  $P4_332$  (# 212) with the lattice constant  $6.563\text{\AA}$ . The unit cell contains four strontium (Sr) atoms and eight silicon (Si) atoms, which occupy the Wyckoff positions 4a and 8c, respectively. The orientation of the atomic positions responsible for handedness in  $\text{SrSi}_2$ . Under a mirror operation, these two structural view in (111) and  $(\bar{1}\bar{1}\bar{1})$  direction, as shown in Fig. 1 (a)-(b), reverse their handedness. This fact can be used to distinguish the two enantiomers of  $\text{SrSi}_2$  crystal. Due to this unique chiral crystal structure,  $\text{SrSi}_2$  lacks both mirror and inversion symmetries, but has  $C_2$ ,  $C_3$  and  $C_4$  rotational symmetries. Since  $\text{SrSi}_2$  is a nonmagnetic system, respecting the time-reversal symmetry, the absence of inversion symmetry is fundamental for realizing a WSM phase with four WNs.

We study the electronic structure in  $\text{SrSi}_2$  using DFT calculations. The Density functional theory (DFT) calculations are based on GGA with the  $\mathbf{k}$ -mesh  $32 \times 32 \times 32$  within the full-potential local-orbital (FPLO) code [57]. The band structures from GGA+SOC along the high symmetry direction in Brillouin zone (BZ) are shown in

TABLE I. Positions, Chern numbers, and energies of the WNs with SOC ( $W_{1,2}$ ) and without SOC ( $V_{1,2}$ ).

| WP    | Position [ $(k_x, k_y, k_z)$ ]<br>in $(\frac{2\pi}{a}, \frac{2\pi}{b}, \frac{2\pi}{c})$ | $C$ | $E$ (meV) |
|-------|---|-----|-----------|
| $V_1$ | $(\pm 0.2001, 0, 0)$  | +1  | -34.4     |
| $V_2$ | $(\pm 0.3691, 0, 0)$  | -1  | 82.3      |
| $W_1$ | $(\pm 0.2003, 0, 0)$  | +2  | -26.3     |
| $W_2$ | $(\pm 0.3696, 0, 0)$  | -2  | 88.2      |

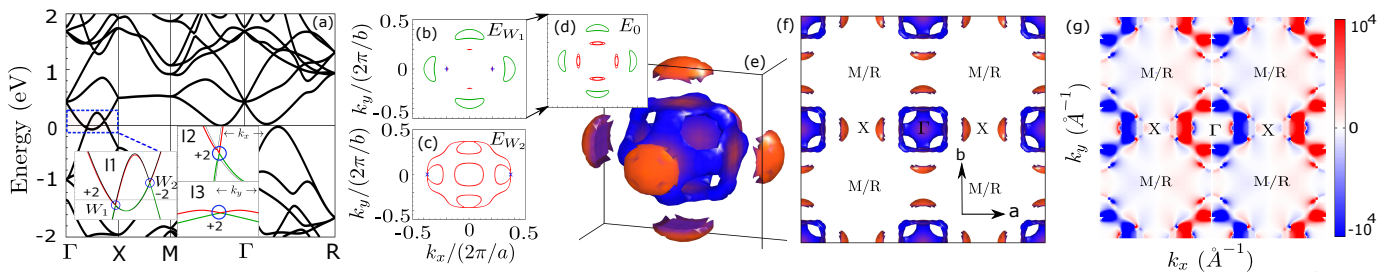


FIG. 2. (a) Bulk band structure of SrSi<sub>2</sub> from GGA+SOC calculation. The energies of the double-WNs are at  $E_{W_1} = -26.3$  meV and  $E_{W_2} = 88.2$  meV associated with topological charge  $n = +2$  and  $n = -2$ , respectively as depicted in inset I1. The insets I2 and I3 demonstrate the linear and quadratic band dispersion, around the WN of chirality  $+2$ , along  $k_x$  and  $k_y$ , respectively. The bulk isoenergy surface for  $k_z = 0$  cut at  $E_f = E_{W_1}$  (b),  $E_f = E_{W_2}$  (c) and  $E_f = 0$  (d). The Weyl points with positive and negative chiralities are marked by  $+$  and  $\times$ , respectively. (e) Three dimensional Fermi surface for a single unit cell and its projection (f) on the  $k_x$ - $k_y$  plane by doubling the unit cell. (g) The  $k_z$  averaged Berry curvature projected on the  $k_x$ - $k_y$  plane.

the Fig. 2 (a). We observe the band crossing between the highest occupied valence bands and the lowest unoccupied conduction along the  $\Gamma - X$  direction. The WNs appear at  $-34.4$  meV ( $V_1$ ) and  $82.3$  meV ( $V_2$ ) with topological charge  $n = +1$  and  $n = -1$ , respectively, without SOC. Under inclusion of SOC, the single WNs change their dispersion to form the double WNs in SrSi<sub>2</sub>. These WNs appear at  $-26.3$  meV ( $W_1$ ) and  $88.2$  meV ( $W_2$ ) with topological charge  $n = +2$  and  $n = -2$  respectively as shown in table I.

The band shown in green (inset Fig. 2(a)) forms the top of the valence band and gives rise to two nested hole pockets along the line  $\Gamma - X$ . Similarly, the band shown in red (inset I1 in Fig. 2(a)) forms the lowest conduction band which results two nested, closed electron pocket centering around the  $\Gamma$  along the direction  $M - \Gamma - X$ . The linear and quadratic nature of the band dispersion along  $k_x$  and  $k_y$  are clearly shown in insets I2 and I3 while focusing on the WN of chirality  $+2$ . Importantly, the WNs of double WSM SrSi<sub>2</sub> in presence of SOC are protected by time reversal and  $C_2$  rotation symmetries while the inversion and mirror symmetries are already broken. Interestingly, in absence of SOC, the quadratic dispersion turns into linear. The size of the electron pockets are larger than the hole pockets. The conventional type-I WSMs are characterized by shrinking of the Fermi surface to a point at the WN energy. The simplest Fermi surface of such a WSM would consist of only two such points. The cut of bulk three dimension Fermi surface for  $k_z = 0$  plane at different energies  $E_f = E_{W_1}$ ,  $0$ , and  $E_{W_2}$  are depicted in Fig. 2 (b), (c) and (d), respectively. There exists only hole (electron) pocket for  $E_f = E_{W_1}$  ( $E_f = E_{W_2}$ ) while Fermi surface hosts both electron and hole pockets simultaneously for any energy  $E_{W_1} < E_f < E_{W_2}$ . The energy separation between these single and double-WNs are  $116.7$  and  $114.5$  meV respectively resulting in interesting chirality related phenomena namely, quantized CPGE response in SrSi<sub>2</sub> which we describe in the subsequent section.

SrSi<sub>2</sub> exhibits a complicated and nested bulk 3D Fermi

surface (see Fig. 2(e)) whose projection in  $k_x - k_y$  plane with the doubling of unit cell along with the high symmetry points of BZ is shown in Fig. 2 (f). We show the  $k_z$  averaged Berry curvature in the  $k_x - k_y$  plane, as depicted in Fig. 2 (f), by summing over all the occupied valence bands till  $E_f = 0$ . The sink ( $C = -2$ ) and source ( $C = 2$ ) of the Berry flux that are marked by blue and red colors respectively in the Fig. 2 (g). The Berry curvature has the negative (positive) flux in the hole pockets along  $\Gamma - X$  ( $\Gamma - \bar{X}$ ) and electron pockets along  $M - \Gamma - R$  ( $\bar{M} - \Gamma - \bar{R}$ ) respectively.

### III. Topological surface states

Figure 3 shows the evolution of the SFS mapping in the (001)-surface with decreasing (increasing) the energy from Fermi level  $E_f = 0$  meV to the WN energy  $E_f = E_{W_1}$  ( $E_f = E_{W_2}$ ) using PYFPLO [57] module as implemented within FPLO via Green's function techniques. We obtain a tight-binding Hamiltonian with 136 bands by projecting the Bloch wave functions onto Wannier functions. Here we consider Sr- 4d, 5s and 5p; Si- 3s and 3p orbitals within the energy range  $-11.6$  eV to  $10.0$  eV. Here we will study the gradual formation of Fermi arcs considering semi-infinite slab geometry. The projection of big electron pocket appears around the  $\Gamma$  point and hole pocket appears along  $\Gamma - X$  direction at  $E_f = 0$  (see Fig. 3 (a)). The surface states are found on the right (left) side for  $k_x > 0$  ( $k_x < 0$ ) in (001)-surface. At  $E_f = 0$ , two Fermi arcs are connected around  $k_x \approx \pm 0.1$  and  $k_x \approx \pm 0.3$  (marked by circle in Fig. 3 (a)) in (001)-surface. With the decreasing energy from  $E_f = 0$  to  $E_f = -10$  meV, the electron pockets around  $\Gamma$  gradually shrinks and the hole pocket along  $\Gamma - X$  increases as shown in Fig. 3 (b). The Fermi arcs get splitted at the point around  $k_x \approx \pm 0.1$  and  $k_x \approx \pm 0.3$  and start to form the long  $S$ -shaped Fermi arcs. Finally at  $E_f = E_{W_1} = -26.3$  meV, the tail of the long  $S$ -shaped Fermi arcs touch the WNs (see fig. 3 (c)). With increas-

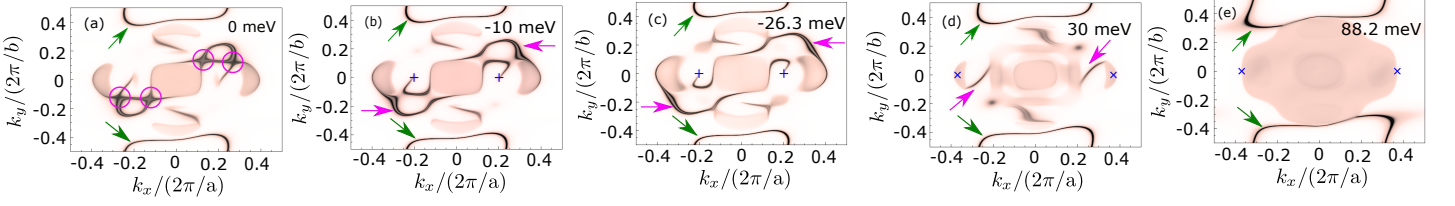


FIG. 3. Surface Fermi surface of (001)-surface from GGA+SOC at (a)  $E_f = 0$ , (b)  $E_f = -10$  meV, (c)  $E_f = -26.3$  meV, (d)  $E_f = 30$  meV, (e)  $E_f = 88.2$  meV. This shows the gradual formation of Fermi arcs i.e., non-trivial surface states (trivial surface states) with the variation of  $E_f$  marked by pink (green) arrows.

ing the Fermi level from  $E_f = 0$  to  $E_f = 30$  meV, the electron pocket increases and hole pocket decreases (see fig. 3 (d)). The Fermi arcs is gradually going into the projected bulk band structure marked by arrows in Fig. 3 (d). At  $E_f = E_{W_2} = 88.2$  meV, the Fermi arcs touching the WNs around  $k_x \approx \pm 0.37$  are submerged into the bulk projected band structure as shown in Fig. 3 (e). Additionally, some trivial surface states running parallel to  $|k_x|$  appear and forms a closed loop. With increasing the Fermi level from  $E_f = 0$ , this trivial surface states touch the electron pockets at  $E_f = 88.2$  meV. The same features in the SFS mapping are also observed for GGA with a singlet Fermi arc instead of Fermi arc doublet.

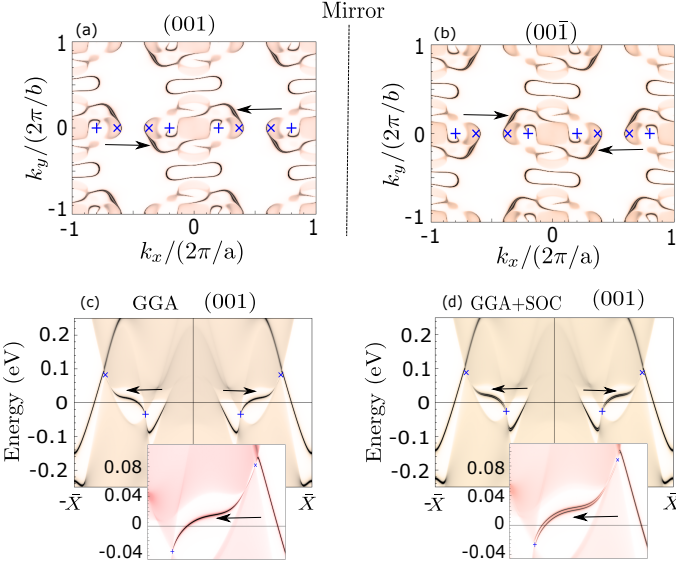


FIG. 4. The surface Fermi surface of (001)-surface (a) and (001 $\bar{1}$ )-surface (b) at  $E_f = E_{W_1}$  respectively. The long “S”-shaped Fermi arcs doublet, marked by arrows, connecting WNs with opposite chirality are found. The surface Fermi surface profiles on (001 $\bar{1}$ )-surface and (001)-surface are related by the mirror reflection but not superimposable on each other. The energy dispersion curve on the (001)-surface along  $\frac{2\pi}{a}(k_x, k_y^{WP}, 0)$  from GGA (c) and GGA+SOC (d) calculations. The long chiral Fermi arcs singlet and doublet are clearly visible for GGA and GGA+SOC and marked by arrows.

To further investigate the nature of the Fermi arc, we calculate the SFS states of (001)- and (001 $\bar{1}$ )-surface re-

spectively as shown in the Fig. 4 (a)-(b) at the WN energy  $E_f = E_{W_2} = -26.3$  meV. Two pair of WNs appear with opposite chirality and are marked by plus (cross) with the topological charge  $n = +2$  ( $n = -2$ ). The non-centrosymmetric compound SrSi $_2$  has two distinct surfaces for (001) and (001 $\bar{1}$ ) due to lack of mirror symmetry (see Fig. 1 (a) and (b)). This causes the SFS profile to possess a handedness that we describe below. We observe a Fermi surface map with a large “S”-shaped Fermi arcs in the full BZ connecting the two WNs of opposite chirality in the (001) surface. Interestingly, the inverted “S”-shaped Fermi arcs are observed in the (001 $\bar{1}$ ) surface. Hence, the orientation of connecting pattern of Fermi arcs becomes reversed in (001)- and (001 $\bar{1}$ )-surface. This property of Fermi surface is related to the enantiomer structure of the material where mirror symmetric counterpart can not be superimposed with the parent structure. We show in Fig. 1 that the two enantiomers of SrSi $_2$  can be distinguished by the handedness of the crystal which is formed by their Sr/Si atoms along the (111) direction. Such a connection between Fermi arcs and crystalline handedness can lead to future studies on transports of chiral topological semimetal and their connection with the structural handedness. Here the Fermi arcs are doubly splitted related to its magnitude of the topological charge  $n = 2$  and marked by arrows in both the Fig. 4 (a)-(b).

To further elucidate the topological structure of the Fermi arcs, we also calculated the energy dispersion curve of the semi-infinite slab for (001)-surface the along the  $\frac{2\pi}{a}(k_x, k_y^{WP}, 0)$  from both GGA and GGA+SOC as shown in the Fig. 4. The Fermi arcs in both cases are formed by a band which connects the top of the valence bands around  $k_x = 0.3$  to the bottom of the conduction around  $k_x = 0.2$  respectively. The Fermi arcs are indicated by the arrows in the Fig. 4 (c)-(d). The singlet and doublet structures of Fermi arc are clearly visible in GGA and GGA+SOC in accordance with the the magnitude of topological charges. The Fermi arc connecting WNs with  $n = \pm 2$  has positive (negative) chirality for  $\Gamma \rightarrow X$  ( $\Gamma \rightarrow -X$ )-direction. This is in stark contrast to the magnetic WSMs where a single Fermi arc connecting two WN of opposite topological charge is observed. The existence of such chiral Fermi arcs for time reversal symmetry broken WSM might lead to distinct transport signatures as compared to the time reversal symmetry

invariant WSM. We also note that the energy dispersion in (00 $\bar{1}$ )-surface can be obtained by mirror reflection on that of the in (001)-surface. Hence the energy dispersion in (00 $\bar{1}$ ) and (001)-surfaces are superimposable with each other. The energy dispersion profile follows a achiral pattern in the above surfaces where surprisingly, non-superimposable chiral nature of SFS profiles are visible.

#### IV. Second order CPGE response

The CPGE injection current is a second order optical response when the system is irradiated with the circularly polarized light. It is defined as

$$\frac{dJ_a}{dt} = \beta_{ab}(\omega) [\mathbf{E}(\omega) \times \mathbf{E}^*(\omega)]_b, \quad (1)$$

where  $\mathbf{E}(\omega) = \mathbf{E}^*(-\omega)$  is the circularly polarized electric field of frequency  $\omega$ ,  $a$  and  $b$  indices are the direction of current  $J_a$  and circular polarized light field respectively. Considering the relaxation time approximation and momentum independent relaxation time  $\tau$  [28, 58, 59], we can introduce the broadening parameter  $\Gamma = \hbar/\tau$ . The conductivity  $\sigma_{ab}^c$  ( $a, b, c = x, y, z$ ) is a third rank tensor representing the photocurrent  $J_c$  generated by electric fields  $E_a$  and  $E_b$ :  $J_c = \sigma_{ab}^c E_a E_b$ . We note that photoconductivity tensor  $\sigma_{ab}^c$  and CPGE tensor  $\beta_{cc}$  are essentially related by relation  $\sigma_{ab}^c = \tau \beta_{cc}$ . From quadratic response theory, the photoconductivity reads as [45, 60–62]:

$$\sigma_{ab}^c(\omega) = \frac{e^3}{\omega^2} \text{Re} \left\{ \phi_{ab} \sum_{\Omega=\pm\omega} \sum_{l,m,n} \int_{BZ} \frac{d^3k}{(2\pi)^3} (f_l^{\vec{k}} - f_n^{\vec{k}}) \right. \\ \left. \times \frac{\langle n_{\vec{k}} | \hat{v}_a | l_{\vec{k}} \rangle \langle l_{\vec{k}} | \hat{v}_b | m_{\vec{k}} \rangle \langle m_{\vec{k}} | \hat{v}_c | n_{\vec{k}} \rangle}{(E_{\vec{k}n} - E_{\vec{k}m} - i\Gamma)(E_{\vec{k}n} - E_{\vec{k}l} - \hbar\Omega - i\Gamma)} \right\} \quad (2)$$

where  $\phi_{ab}$  is the phase difference between the driving field  $E_a$  and  $E_b$ . Here,  $|n_{\vec{k}}\rangle$ ,  $E_{\vec{k}n}$ ,  $m_0$ , and  $\hat{v}_b = \hat{p}/m_0$  are electronic state, associated energy, free-electron mass and quasi-particle velocity operator along  $b$ -direction, respectively. For circularly (linearly) polarized light,  $\phi_{ab}$  becomes imaginary (real). We note that  $\phi_{ab} = i$  and  $-i$ , correspond to right and left circularly polarized light, respectively. Hence, the photocurrent along  $c$ -direction changes its sign under the reversal of polarization of the light having electric fields along  $a$  and  $b$ -direction [45]. For example, one can consider the polarization vector  $(0, 1, i)$  and  $(0, 1, -i)$  for right and left circularly polarized light. Once the polarization of the circularly polarized light changes, the relative phases between the electric fields  $E_y$  and  $E_z$  also changes such that  $\phi_{yz} = i \rightarrow -i$  and eventually leading to the reversal in the direction for the photocurrent  $J_x$ . The imaginary (real) part of the integral in Eq. (2) describes the CPGE (shift current response) under circularly (linearly) polarized light [63, 64].

We now discuss the photoconductivity formula as given in Eq. (2) in more detail. The formula is based on the three band transition where an additional virtual band is

considered in addition to valence and conduction band. The three band transitions are given by  $n \rightarrow m \rightarrow l$  and  $l \neq m$ , whereas, two band transitions are given by  $l = m$ . It has been found that the two-band real transitions contribute much less in photocurrent as WN contributes maximally. On the other hand, virtual transitions from the occupied Weyl to the empty Weyl band via a third trivial band predominantly contribute to the high value of shift current and CPGE [45]. At the same time, we note that quantized CPGE responses are observed in various model systems without inversion symmetry employing the two band formula for CPGE that we discuss at the end of this section [4, 30, 53].

We below probe the behavior of photocurrent by plausible analytical argument. At the outset, we note that imaginary part of velocity numerator  $N = \langle n_{\vec{k}} | \hat{v}_a | l_{\vec{k}} \rangle \langle l_{\vec{k}} | \hat{v}_b | m_{\vec{k}} \rangle \langle m_{\vec{k}} | \hat{v}_c | n_{\vec{k}} \rangle$  would survive after the integral for time reversal symmetry invariant non-magnetic WSM. Since the real part of the photoconductivity formula Eq. (2) gives the CPGE current, the energy denominator  $D = (E_{\vec{k}n} - E_{\vec{k}m} - i\Gamma)(E_{\vec{k}n} - E_{\vec{k}l} + \hbar\Omega - i\Gamma)$  has to be real under this circumstances. The momentum integration in Eq. (2) acquires imaginary values for CPGE photoconductivity. One can continue the calculation of photoconductivity by retaining the real part of  $D$  as  $\text{Re}[D] = -\delta(E_{\vec{k},n} - E_{\vec{k},m})/\Gamma$ . We note that  $\delta(E_{\vec{k},n} - E_{\vec{k},m})$  comes from the imaginary part of  $(E_{\vec{k}n} - E_{\vec{k}m} - i\Gamma)^{-1}$  and the term  $1/\Gamma$  arises from the second part  $(E_{\vec{k}n} - E_{\vec{k}l} + \hbar\Omega - i\Gamma)^{-1}$  due to the selection rule  $E_{\vec{k}n} = E_{\vec{k}l} - \hbar\Omega$ . We know that CPGE receives the contribution from closed optically activated momentum surface as mediated by  $\delta$ -functions [4, 53]. The momentum integration of  $N/D$  becomes imaginary for the CPGE photocurrent. Considering the time reversal symmetry invariant nature of the material and type of polarization, one can perform the the momentum integration by taking into account the appropriate terms only. Then the photoconductivity can be rewritten in the following

approximated form

$$\begin{aligned}
& \sigma_{ab}^c(\omega) \\
&= \frac{e^3}{\omega^2} \text{Re} \left[ \phi_{ab} \sum_{\Omega=\pm\omega} \sum_{l,n,m} \int \frac{d^3k}{(2\pi)^3} f_{nl}^{\vec{k}} \right. \\
& \quad \left. \frac{\langle n_{\vec{k}} | \hat{v}_a | l_{\vec{k}} \rangle \langle l_{\vec{k}} | \hat{v}_b | m_{\vec{k}} \rangle \langle m_{\vec{k}} | \hat{v}_c | n_{\vec{k}} \rangle}{(E_{\vec{k}n} - E_{\vec{k}m} - i\Gamma)(E_{\vec{k}n} - E_{\vec{k}l} - \hbar\Omega - i\Gamma)} \right] \\
&\approx -\frac{e^3}{\omega^2} \left[ \sum_{\Omega=\pm\omega} \sum_{l,n,m} \int \frac{d^3k}{(2\pi)^3} f_{nl}^{\vec{k}} \delta(E_{\vec{k}n} - E_{\vec{k}m}) \right. \\
& \quad \left. \frac{\langle n_{\vec{k}} | \hat{v}_a | l_{\vec{k}} \rangle \langle l_{\vec{k}} | \hat{v}_b | m_{\vec{k}} \rangle \langle m_{\vec{k}} | \hat{v}_c | n_{\vec{k}} \rangle}{(E_{\vec{k}n} - E_{\vec{k}l} - \hbar\Omega - i\Gamma)} \right] \\
&\approx -\frac{e^3}{\omega^2} \left[ \sum_{\Omega=\pm\omega} \sum_{l,n} \int \frac{d^3k}{(2\pi)^3} f_{nl}^{\vec{k}} \frac{\langle n_{\vec{k}} | \hat{v}_a | l_{\vec{k}} \rangle \langle l_{\vec{k}} | \hat{v}_b | n_{\vec{k}} \rangle \langle n_{\vec{k}} | \hat{v}_c | n_{\vec{k}} \rangle}{(E_{\vec{k}n} - E_{\vec{k}l} - \hbar\Omega - i\Gamma)} \right. \\
& \quad \left. \frac{E_{\vec{k},nl}^2 R_{\vec{k},nl}^c \partial_{k_c} E_{\vec{k}n}}{(E_{\vec{k}n} - E_{\vec{k}l} - \hbar\Omega - i\Gamma)} \right] \\
&\approx -\frac{e^3}{\hbar^2 \omega^2} \left[ \sum_{\Omega=\pm\omega} \sum_{l,n} \int \frac{k^2 dk_c d\Sigma}{(2\pi)^3} f_{nl}^{\vec{k}} \frac{E_{\vec{k},nl}^2 R_{\vec{k},nl}^c \partial_{k_c} E_{\vec{k}n}}{(E_{\vec{k}n} - E_{\vec{k}l} - \hbar\Omega - i\Gamma)} \right] \\
&\approx -\frac{e^3}{\hbar^2 \omega^2} \left[ \sum_{\Omega=\pm\omega} \sum_{l,n} \int \frac{dE_{\vec{k}} d\Sigma}{(2\pi)^3} \frac{E_{\vec{k},nl}^2 k^2 R_{\vec{k},nl}^c}{(E_{\vec{k}n} - E_{\vec{k}l} - \hbar\Omega - i\Gamma)} \right] \\
&\approx -\frac{e^3 \tau}{\hbar \omega^2} \sum_{\Omega=\pm\omega} \sum_{l,n} \int \frac{d\Sigma}{(2\pi)^3} \Omega^2 k^2 R_{\vec{k},nl}^c \\
&\approx -\beta_0 \tau \sum_{l,n} \int dS_{\vec{k},nl} R_{\vec{k},nl} \\
&\approx i\beta_0 \tau \sum_n \int d\vec{S}_n \cdot \vec{\Omega}_n \\
&\approx iC\beta_0 \tau
\end{aligned}$$

where  $C = \sum_n C_n$  is Chern number summing over all the occupied bands and  $\beta_0 = e^3/\hbar$ .

Considering the relaxation time approximation for diffusive transport, the relation between the broadening parameter  $\Gamma$  and the quasiparticle lifetime  $\tau$  is given by  $\Gamma = \hbar/\tau$  for metallic systems [28, 45, 58, 59]. In the above derivation, we first combine  $\phi_{ab} \times (E_{\vec{k},n} - E_{\vec{k},m} - i\Gamma)^{-1}$  as  $-\delta(E_{\vec{k},n} - E_{\vec{k},m})$  to retain the real part. Thereafter, we remove  $\text{Re}[\dots]$  considering the fact that integration of  $\frac{\langle n_{\vec{k}} | \hat{v}_a | l_{\vec{k}} \rangle \langle l_{\vec{k}} | \hat{v}_b | m_{\vec{k}} \rangle \langle m_{\vec{k}} | \hat{v}_c | n_{\vec{k}} \rangle}{(E_{\vec{k},n} - E_{\vec{k},l} - \hbar\Omega - i\Gamma)}$  yields quantized contributions to CPGE. To be precise, the terms  $\text{Im}[\langle n_{\vec{k}} | \hat{v}_a | l_{\vec{k}} \rangle \langle l_{\vec{k}} | \hat{v}_b | m_{\vec{k}} \rangle \langle m_{\vec{k}} | \hat{v}_c | n_{\vec{k}} \rangle]$  and  $\text{Im}[(E_{\vec{k},n} - E_{\vec{k},l} - \hbar\Omega - i\Gamma)]$  combine together allowing the quantized contribution to CPGE within the closed optically activated momentum surface. We below demonstrate the technical steps with plausible arguments.

The topological charges of the activated WNs contribute to the quantization of photoconductivity. We consider the selection rule  $E_{\vec{k},nl} = E_{\vec{k},l} - E_{\vec{k},n} = \hbar\Omega$ , owing to the optically activated momentum surface, and  $f_{nl}^{\vec{k}} = f_n^{\vec{k}} - f_l^{\vec{k}}$  are difference between band energies and

Fermi-Dirac distributions, and  $r_{\vec{k},nl}^a = i \langle l_{\vec{k}} | \partial_{k_a} | n_{\vec{k}} \rangle = i \frac{\hbar \hat{v}_{\vec{k},nl}^a}{E_{\vec{k},nl}}$ . For  $n \neq l$ ,  $r_{\vec{k},nl}^a$  are the interband position matrix elements or off-diagonal Berry connection. For  $n = l$ ,  $r_{\vec{k},nn}^a$  is the diagonal Berry connection. For the general case with  $n \neq l$ ,  $R_{\vec{k},nl}^c = \epsilon_{abc} r_{\vec{k},nl}^a r_{\vec{k},ln}^b$ . We note that  $\langle n_{\vec{k}} | \hat{v}_a | l_{\vec{k}} \rangle \langle l_{\vec{k}} | \hat{v}_b | n_{\vec{k}} \rangle$ , coming from the imaginary numerator as described above, can be written as  $E_{\vec{k},nl}^2 R_{\vec{k},nl}^c$ . On the other hand, the energy integration  $\int dE_{\vec{k}} [\frac{E_{\vec{k},nl}^2}{(E_{\vec{k},n} - E_{\vec{k},l} - \hbar\Omega - i\Gamma)}]$ , assuming the imaginary part of denominator contributes to CPGE, reduces to  $\frac{\hbar^2 \Omega^2}{\Gamma}$ . Upon judiciously implementing all the above mathematical steps, one can bring down the quantity  $\int dk_c [\frac{\langle n_{\vec{k}} | \hat{v}_a | l_{\vec{k}} \rangle \langle l_{\vec{k}} | \hat{v}_b | n_{\vec{k}} \rangle \partial_{k_c} E_{\vec{k},n}}{(E_{\vec{k},n} - E_{\vec{k},l} - \hbar\Omega - i\Gamma)}]$  to the following form  $\frac{\hbar^2 \Omega^2 R_{\vec{k},nl}^c}{\Gamma}$ . The relation between  $\vec{R}_{\vec{k},nl}$  and Berry curvature is given by  $\vec{\Omega}_{\vec{k},n} = i \sum_{l \neq n} \vec{R}_{\vec{k},nl}$ . Here  $\vec{S}_n$  is a closed surface of band  $n$  enclosing the degenerate points. For a given frequency  $\omega$ , the delta function and Fermi-Dirac distributions select a surface  $\vec{S}_{nl}$  in the  $\vec{k}$  space where  $d\vec{S} = k^2 d\Sigma$  denotes the surface element oriented normal to  $\vec{S}$  where  $d\Sigma$  is the differential solid angle. Therefore, the CPGE current is essentially the Berry flux penetrating through surface  $\vec{S}$ . We note that trace of CPGE tensor  $\text{Tr}[\beta]/i\beta_0$  is found to be quantized [4, 30, 53].

We now derive the two-band formula for the photocurrent  $\tilde{\sigma}_{ab}^c(\omega)$  from three-band formula by accounting the direct optical transition from  $|l_{\vec{k}}\rangle$  to  $|n_{\vec{k}}\rangle$  as given in Eq. (2). We consider  $n = m$  and  $(E_{\vec{k},n} - E_{\vec{k},m} - i\Gamma)^{-1} = i/\Gamma = i\tau/\hbar$ . One can allow a broadening  $\Gamma$  around a given energy level  $E_{\vec{k},n}$ . This comes into play when any two energy levels become equal to each other within the quantum limit. Using  $E_{\vec{k},nl} = \pm\hbar\omega$ , can write  $r_{\vec{k},nl}^a = i \frac{\hbar \hat{v}_{\vec{k},nl}^a}{E_{\vec{k},nl}} = i \frac{\hat{v}_{\vec{k},nl}^a}{\omega}$ . The photoconductivity as reduced from Eq. (2), is given below [4, 5, 65]

$$\tilde{\sigma}_{ab}^c(\omega) = \frac{e^3 \tau}{\hbar} \epsilon_{bfg} \sum_{l,n} \int_{BZ} \frac{d^3k}{(2\pi)^3} f_{nl}^{\vec{k}} \Delta_{\vec{k},nl}^a r_{\vec{k},nl}^f r_{\vec{k},ln}^g \delta(\hbar\omega - E_{\vec{k},nl}) \quad (4)$$

with  $\hat{v}_{\vec{k},nl}^f = \langle n_{\vec{k}} | \hat{v}_f | l_{\vec{k}} \rangle$ ,  $E_{\vec{k},nl} = E_{\vec{k},n} - E_{\vec{k},l}$  and  $\Delta_{\vec{k},nl}^a = \hat{v}_{\vec{k},nn}^a - \hat{v}_{\vec{k},ll}^a$ . Notice that  $\epsilon_{bfg}$  represents the Levi-Civita symbol and two band formula for photoconductivity is usually referred to as  $\tilde{\sigma}_{ab}(\omega)$  in the literature. Here we have already considered  $\phi_{ab} = i$  while computing the two band formula Eq. (4) from three band formula Eq. (2). One there has to be careful with the summation  $\sum_{l,n} f_{nl}^{\vec{k}} \hat{v}_{\vec{k},nl}^a \hat{v}_{\vec{k},ln}^b \hat{v}_{\vec{k},nn}^c$ . We below discuss the analytical reduction from three band formula (Eq. (2)) to two band with plausible argument.

The summation is over the repeated indices, and  $l(n) \rightarrow n(l)$ , one can find  $f_{nl}^{\vec{k}} \hat{v}_{\vec{k},nl}^a \hat{v}_{\vec{k},ln}^b \hat{v}_{\vec{k},nn}^c \rightarrow$

$f_{ln}^{\vec{k}} \hat{v}_{\vec{k},ln}^a \hat{v}_{\vec{k},nl}^b \hat{v}_{\vec{k},ll}^c$ . The term  $\hat{v}_{\vec{k},nl}^a \hat{v}_{\vec{k},ln}^b$  can be written in an anti-symmetric way  $A(a,b) = \frac{1}{2}(\hat{v}_{\vec{k},nl}^a \hat{v}_{\vec{k},ln}^b - \hat{v}_{\vec{k},ln}^a \hat{v}_{\vec{k},nl}^b)$  such that  $A(a,b)$  reverse its sign under the reversal of polarization  $A(a,b) = -A(b,a)$  with  $a(b) \rightarrow b(a)$ . Now, we can decompose the summation with  $l(n) \rightarrow n(l)$  and find  $\sum_{n,l} \frac{1}{2} \left[ f_{nl}^{\vec{k}} A(a,b) \hat{v}_{\vec{k},nn}^c + f_{ln}^{\vec{k}} A(a,b) \hat{v}_{\vec{k},ll}^c \right] = \sum_{n,l} \left[ f_{nl}^{\vec{k}} \frac{(\hat{v}_{\vec{k},nl}^a \hat{v}_{\vec{k},ln}^b - \hat{v}_{\vec{k},ln}^a \hat{v}_{\vec{k},nl}^b)}{2} \Delta_{\vec{k},nl}^c \right]$  with  $\Delta_{\vec{k},nl}^c = \partial_{k_c} E_{\vec{k},nn} - \partial_{k_c} E_{\vec{k},ll} = \hat{v}_{\vec{k},nn}^c - \hat{v}_{\vec{k},ll}^c$  and  $f_{nl}^{\vec{k}} = -f_{ln}^{\vec{k}}$ . As a result, the two-band photoconductivity formula looks like

$$\tilde{\sigma}_{ab}^c(\omega) = \frac{e^3 \tau}{\omega^2 \hbar} \sum_{\Omega=\pm\omega} \sum_{l,n} \int \frac{d^3 k}{(2\pi)^3} f_{nl}^{\vec{k}} \frac{1}{2} (\hat{v}_{\vec{k},nl}^a \hat{v}_{\vec{k},ln}^b - \hat{v}_{\vec{k},ln}^a \hat{v}_{\vec{k},nl}^b) \times \Delta_{\vec{k},nl}^c \delta(E_{\vec{k},nl} - \hbar\Omega) \quad (5)$$

In order to cast the above expression in terms of  $r_{\vec{k},nl}^{a,b}$ , one has to use  $\hat{v}_{\vec{k},nl}^{a,b} = -i r_{\vec{k},nl}^{a,b} E_{\vec{k},nl} / \hbar$  with the selection rule  $E_{\vec{k},nl} = \pm \hbar\omega$ , provided  $E_{\vec{k},nl} = \hbar\Omega$ , in accordance with the delta function  $\delta(E_{\vec{k},nl} - \hbar\omega)$ . Therefore, by replacing  $\delta(E_{\vec{k},nl} - \hbar\omega)$  with  $\delta(E_{\vec{k},nl} - \hbar\omega)$ , and absorbing the summation over  $\Omega = \pm\omega$ , the photoconductivity is found to be

$$\tilde{\sigma}_{ab}^c(\omega) = \frac{e^3 \tau}{\hbar} \sum_{l,n} \int_{BZ} \frac{d^3 k}{(2\pi)^3} f_{nl}^{\vec{k}} [r_{\vec{k},nl}^a r_{\vec{k},ln}^b - r_{\vec{k},ln}^a r_{\vec{k},nl}^b] \Delta_{ln}^c \delta(E_{\vec{k},nl} - \hbar\omega) \quad (6)$$

with  $[r_{\vec{k},nl}^a, r_{\vec{k},ln}^b] = (r_{\vec{k},nl}^a r_{\vec{k},ln}^b - r_{\vec{k},ln}^a r_{\vec{k},nl}^b) / 2$ . One can thus obtain two band CPGE formula Eq. (4), starting from the three band approach, where the reversal of polarization appropriately leads to a reversal in sign  $\tilde{\sigma}_{ab}^c(\omega) = -\tilde{\sigma}_{ba}^c(\omega)$  owing to the above commutator like relation  $[r_{\vec{k},nl}^a, r_{\vec{k},ln}^b] = -[r_{\vec{k},nl}^b, r_{\vec{k},ln}^a]$ . We note that Eqs. (6) and (4) are connected by appropriate rearrangement of indices in Levi-Civita symbol. We below examine the quantization in the photoconductivity from the three and two band approaches.

According to symmetry classification of the material, the non zero elements of the CPGE tensor for SrSi<sub>2</sub> are  $\sigma_{yz}^x, \sigma_{zx}^y, \sigma_{xy}^z$ . To be precise,  $\sigma_{yz}^x = -\sigma_{zx}^y = \sigma_{xy}^z$ . The relaxation time plays important role in determining the quantization of CPGE. Therefore it is indeed very important to have correct estimation of relaxation time to obtain reliable CPGE. Typically, the hot-electron scattering time for metallic systems  $\approx fs$  [29] which corresponds to a broadening parameter  $\Gamma = \hbar/\tau = 10 - 100$  meV. The effect of temperature and impurity scattering on photocurrent generation are taken into account by this broadening parameter  $\Gamma$ . The BZ was sampled by  $\mathbf{k}$ -mesh with  $250 \times 250 \times 250$  to compute the CPGE current.

Figure 5 (a)-(b) and (c)-(d) shows the CPGE response for  $\Gamma = 10, 100$  meV with and without SOC respectively. We find the chiral chemical potential  $\mu_{ch} =$

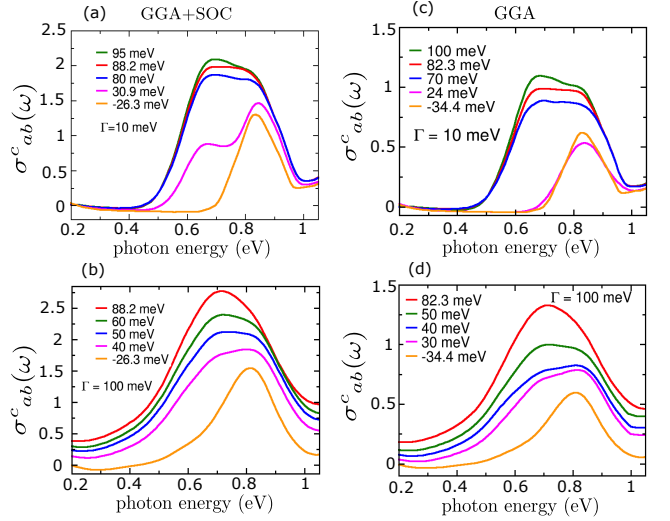


FIG. 5. CPGE, computed from Eq. (2), with GGA (a)-(b) and GGA+SOC (c)-(d) for broadening parameter  $\Gamma = 10$  meV and  $\Gamma = 100$  meV respectively. We plot  $\sigma_{ab}^c = \sigma_{ab}^c / i$  in all the figures. The different colored lines correspond to different chemical potentials as denoted in the figures. The red (orange) line in each figures represents the CPGE response when  $E_f$  is set at energy associated with WN of negative (positive) chirality.

$E_{V_2} - E_{V_1} = 116.7 (= E_{W_2} - E_{W_1} = 114.5)$  meV for GGA (GGA+SOC) calculations. The magnitude of topological charge changes whether SOC is excluded or included in the DFT calculation. This is clearly reflected in the quantization of photoconductivity while studied it in presence and absence of SOC i.e., photoconductivity is found to be quantized around the value 1 (2) for GGA (GGA+SOC) calculations. The magnitude of the quantization is governed by the topological charge of the activated WN. This is in accordance with the theoretical conjecture as discussed in the earlier section. With inclusion of SOC, we further observe the quantization within the energy  $\approx 0.6 < \omega < 0.9$  eV is very prominent compared to the GGA results when the Fermi level is kept near one of the WNs at  $E_f = E_{W_2} = 88.2$  meV for  $\Gamma = 10$  meV as shown in Fig.5 (a). The  $\sigma_{yz}^x$  and  $\sigma_{zx}^z$  components of CPGE response follow the same sign of the activated WN at  $E_{W_2} = 88.2$  meV ( $n = -2$ ) whereas the  $\sigma_{yz}^y$  reverses its sign.

The frequency windows for quantization is given by  $2|E'_{W_1}| < \omega < 2|E'_{W_2}|$  with  $E'_{W_1, W_2} = E_{W_1, W_2} - E_f$ . For,  $E_f = 88.2$  meV, the frequency window for quantization becomes  $0 < \omega < 0.3$  eV that does not match with our numerical findings. However, the extent of frequency interval within which quantization occurs i.e., 0.3 eV, predicted from analytical analysis, matches well with the numerical finding. We find that the quantization starts around  $\omega \simeq 0.6$  eV which can be due to the presence of other bands lying in the vicinity of WN energies  $E_{W_2}$  and  $E_{W_1}$  and their non-linear dispersive nature. The quantization within a given frequency window can only be

predicted by the low-energy mode. On the other hand, in real material there exist a variety of non-linear and non-trivial effects causing the deviation from the exact quantization.

We observe a deviation from quantization for  $E_f = 95.0, 80.0$  meV away from the WN energies. Interestingly, when we keep the Fermi level near other WN (with topological charge  $n = 2$ ) energy at  $E_{W_2} = -26.3$  meV, a non-zero but non quantized response of CPGE is observed. It is expected that WN with  $n = +2$  will contribute to the photoconductivity. We observe qualitatively the same behavior for  $E_f = 30.9$  meV,  $E'_{W_1} = E'_{W_2}$  i.e., the Fermi level is exactly at midway between two WN energies. These results are qualitatively different from a time reversal symmetry broken WSMs where CPGE responses are quantized to two opposite values depending on the topological charge of the activated WN at a given Fermi level [4]. On the other hand, CPGE response for time reversal symmetry invariant WSM is found to be different from time reversal symmetry broken WSM as the Berry curvature and velocity exhibit non-trivial behavior over BZ. We here find similar agreement in CPGE response for the non-magnetic material SrSi<sub>2</sub>. We obtain similar findings with GGA calculations as shown in Fig. 5 (c) and (d). We note that with increasing broadening parameter  $\Gamma$ , the quantization of photoconductivity is lost and it can acquire values more than the magnitude of topological charge (see Fig. 5 (b) and (d)). This is due to the fact that more states contribute to the photoconductivity around a given Fermi level. Therefore, photoconductivity exhibits quantization only when  $\Gamma$  is less than the energy difference between two consecutive bands around a given Fermi energy in the vicinity of WN energy.

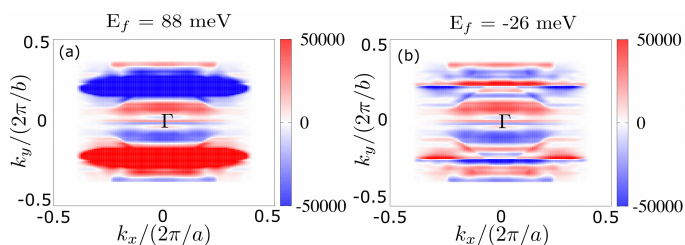


FIG. 6. Momentum resolved  $k_z$ -averaged photoconductivity considering  $\omega = 0.75$  eV for two energies at (a)  $E_f = 88.2$  meV and (b)  $E_f = -26.3$  meV respectively associated with WNs of opposite chirality .

To understand the distinct behavior of photoconductivity around two WNs in different energies  $E_f = 88.2, -26.3$  meV, we analyze the momentum resolved structure of CPGE conductivity as shown in Fig. 6 (a) and (b). We evaluate Eq. (2) as a function of  $k_x$  and  $k_y$ , integrating over  $k_z$ , at a given value of  $\omega = 75.0$  meV for which photoconductivity becomes quantized. We find that the structure of the momentum resolved photoconductivity for  $E_f = 88.2$  meV is substantially different from that of the for  $E_f = -26.3$  meV. These two differ-

ent momentum distributions at two WNs with opposite chirality clearly refers to the fact that CPGE will not be opposite of each other for these two WNs. This is due to the fact that the Berry curvature and velocity, essentially determining the response, behave differently at the two WNs with opposite chirality for time reversal symmetric systems [53].

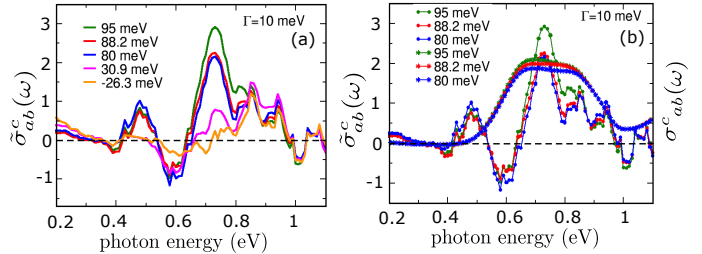


FIG. 7. (a) CPGE from 2-band approach Eq. (4) with SOC using the Lorentzian broadening parameter  $\Gamma = 10$  meV while numerically implementing  $\delta(\hbar\omega - E_{\vec{k},nl}^-)$  [28]. (b) Comparison of CPGE response from 2-band (marked by circle) and 3-band (marked by star) approach using the same broadening parameter respectively. We plot  $\tilde{\sigma}_{ab}^c(\omega) = \tilde{\sigma}_{ab}^c/i$  in all the figures. The different colored lines correspond to different chemical potentials as designated in the figures.

We now compare our findings, followed by three band formula (Eq. (2)), with the two band formula (Eq. (4)) as shown in Fig. 7 (a) and (b), considering GGA+SOC calculations. It is evident that there is no quantization observed from two band formula suggesting the important role played by the virtual transition channel as incorporated in the three band formula. However, the CPGE, obtained from Eq. (4) becomes qualitatively pronounced within the same frequency window for which quantization observed following Eq. (2). On the other hand, we commonly observe that CPGE are not opposite of each other for  $E_f = 88.2$  meV and  $E_f = -26.3$  meV. Therefore, in order to predict the correct behavior as far as the quantization is concerned, the three band formula is found to be useful in examining the optical responses of semimetals [63].

We here compare with the quantized CPGE response for multifold fermion transition metal mono-silicides, with higher spin degrees of freedom, where multiple bands show linear band crossing at the degenerate points [5]. By contrast, SrSi<sub>2</sub>, with an effective spin-1/2 degrees of freedom, exhibits non-linear band crossing at the WNs in presence of SOC. However, in both the materials, the inversion and mirror symmetries are broken resulting in non-degenerate WNs with finite chiral chemical potential. The quantized response in CPGE is a consequence of that while non-centrosymmetric WSM TaAs with degenerate WNs shows non-quantized CPGE response [45]. Therefore, the linear band dispersion along at least one momentum around the gap closing point, noticed for all of the above materials, might not be directly responsible for the quantized response unless there exist finite chiral chemical potential. Having said that, we note that



the magnitude of quantization depends on the underlying topological structure of these materials.

In the case of multifold fermions, to be precise, the higher spin degrees of freedom essentially leads to the higher order topological charge. The optically activated momentum surface might include more than a single band. This equivalently results in the quantized CPGE trace coming from the Berry curvatures associated with more than a single band. Therefore, Chern numbers, associated with the various activated topological bands (i.e., within the optically activated momentum surface) are essentially responsible for the high value of quantization for CPGE trace in multifold fermions [5]. On the other hand, the quadratic energy dispersion of SrSi<sub>2</sub> with SOC (see Fig. 2 (a)) imprints its signature in the quantized CPGE trace via the topological charge even though it does not have more than twofold degeneracy or higher spin degrees of freedom as found in multifold fermion. The Berry curvature of a single band, within the optically activated momentum surface, would contribute to the quantized CPGE trace in double WSM SrSi<sub>2</sub>. This is in contrast to the multifold fermions where Berry curvatures, coming from different bands can add up to give rise the high value of quantized CPGE trace.

The quantization in multifold fermions is observed following the two band formula (Eq. (4)) [5] while the quantization in present case of double WSM is based on the three band formula (Eq. (2)). This is apparently very much intriguing and it requires extensive future investigations. However, the deviation from quantization following two band formula in the present case, is not related to the broadening parameter as this parameter appears both in two band as well as three band formulas. It might be that the three band approach is able mimic the effect of anisotropic non-linear bands in double WSM more vividly than the two band approach. Therefore, it would be really an interesting future direction to systematically explore the photoconductivity in various other suitable materials.

## V. Conclusions

To summarize, considering SrSi<sub>2</sub> as a non-centrosymmetric and non-magnetic double-WSM we first study the structural handedness to show enantiomeric nature of the material. This manifests itself through the SFS profile in (001) and (00 $\bar{1}$ ) surface. The large  $S$  [inverted  $S$ ] shaped Fermi arcs in the high symmetry direction  $\Gamma - X$  for (001) [(00 $\bar{1}$ )] surface referring to the mirror symmetric but not superimposable nature of SFS between (001) [(00 $\bar{1}$ )] surfaces. On the other hand, bulk Fermi surface depicts the emergence of electron and hole pocket suggesting type-I nature of the WSM. We perform GGA and GGA+SOC calculations to examine the topological properties of the material from surface energy spectrum where we find singlet and doublet chiral Fermi arc, respectively. Unlike the SFS, the surface energy dispersion between (001) and (00 $\bar{1}$ ) surfaces are mirror symmetric as well as superimposable with respect to each other. The enantiomeric property of the material thus leads to a chiral SFS and an achiral surface energy dispersion.

Having investigated the connection between structural handedness and chirality of surface Fermi surface profiles, we now study the CPGE as there exists a substantial gap between the energies of WNs with opposite chirality. The CPGE shows a quantized plateau depending on the topological charge of the activated WN when Fermi level is set only around the WN with higher energy. This is markedly different from the time reversal symmetry breaking WSM where CPGE is quantized to two exactly opposite plateau, depending on the topological charge of the respective activated WN, for two different energies. We analyze the momentum resolved structure of CPGE at the two different WN energies to strengthen our findings. We additionally compare our results with the two-band formula to show that three-band formula captures the virtual transitions from Weyl bands to trivial bands in determining the accurate photocurrent responses.

## VI. Acknowledgments

BS thanks Jeroen van den Brink, Yang Zhang, Yan Sun for discussions and Ulrike Nitzsche for technical assistance. The calculations were carried out in the IFW cluster. We sincerely acknowledge the anonymous referees for their constructive suggestions.

- 
- [1] J. Ma and D. A. Pesin, *Phys. Rev. B* **92**, 235205 (2015).
  - [2] J. B. Pendry, *Science* **306**, 1353 (2004).
  - [3] E. M. Carnicom, W. Xie, T. Klimczuk, J. Lin, K. Górnicka, Z. Sobczak, N. P. Ong, and R. J. Cava, *Science advances* **4**, eaar7969 (2018).
  - [4] F. de Juan, A. G. Grushin, T. Morimoto, and J. E. Moore, *Nature communications* **8**, 15995 (2017).

- [5] F. Flicker, F. De Juan, B. Bradlyn, T. Morimoto, M. G. Vergniory, and A. G. Grushin, *Physical Review B* **98**, 155145 (2018).
- [6] F. de Juan, Y. Zhang, T. Morimoto, Y. Sun, J. E. Moore, and A. G. Grushin, *Physical Review Research* **2**, 012017 (2020).

- [7] C.-K. Chan, N. H. Lindner, G. Refael, and P. A. Lee, *Physical Review B* **95**, 041104 (2017).
- [8] S. Zhong, J. E. Moore, and I. Souza, *Physical Review Letters* **116**, 077201 (2016).
- [9] G. Rikken, J. Fölling, and P. Wyder, *Physical Review Letters* **87**, 236602 (2001).
- [10] T. Morimoto and N. Nagaosa, *Physical Review Letters* **117**, 146603 (2016).
- [11] A. Bogdanov and A. Hubert, *Journal of magnetism and magnetic materials* **138**, 255 (1994).
- [12] G. S. Jenkins, C. Lane, B. Barbiellini, A. B. Sushkov, R. L. Carey, F. Liu, J. W. Krizan, S. K. Kushwaha, Q. Gibson, T.-R. Chang, H.-T. Jeng, H. Lin, R. J. Cava, A. Bansil, and H. D. Drew, *Physical Review B* **94**, 085121 (2016).
- [13] S. Borisenko, Q. Gibson, D. Evtushinsky, V. Zabolotnyy, B. Büchner, and R. J. Cava, *Physical Review Letters* **113**, 027603 (2014).
- [14] H. Weyl, *Zeitschrift für Physik* **56**, 330 (1929).
- [15] N. P. Armitage, E. J. Mele, and A. Vishwanath, *Reviews of Modern Physics* **90**, 015001 (2018).
- [16] N. Nagaosa, J. Sinova, S. Onoda, A. H. MacDonald, and N. P. Ong, *Reviews of modern physics* **82**, 1539 (2010).
- [17] D. Xiao, M.-C. Chang, and Q. Niu, *Reviews of modern physics* **82**, 1959 (2010).
- [18] B. Yan and C. Felser, *Annual Review of Condensed Matter Physics* **8**, 337 (2017).
- [19] N. Armitage, E. Mele, and A. Vishwanath, *Reviews of Modern Physics* **90**, 015001 (2018).
- [20] S.-Y. Xu, I. Belopolski, N. Alidoust, M. Neupane, G. Bian, C. Zhang, R. Sankar, G. Chang, Z. Yuan, C.-C. Lee, *et al.*, *Science* **349**, 613 (2015).
- [21] B. Lv, N. Xu, H. Weng, J. Ma, P. Richard, X. Huang, L. Zhao, G. Chen, C. Matt, F. Bisti, *et al.*, *Nature Physics* **11**, 724 (2015).
- [22] B. Lv, H. Weng, B. Fu, X. P. Wang, H. Miao, J. Ma, P. Richard, X. Huang, L. Zhao, G. Chen, *et al.*, *Physical Review X* **5**, 031013 (2015).
- [23] G. Xu, H. Weng, Z. Wang, X. Dai, and Z. Fang, *Physical Review Letters* **107**, 186806 (2011).
- [24] C. Fang, M. J. Gilbert, X. Dai, and B. A. Bernevig, *Physical Review Letters* **108**, 266802 (2012).
- [25] B.-J. Yang and N. Nagaosa, *Nature communications* **5**, 4898 (2014).
- [26] N. B. Schröter, D. Pei, M. G. Vergniory, Y. Sun, K. Manna, F. De Juan, J. A. Krieger, V. Süß, M. Schmidt, P. Dudin, *et al.*, *Nature Physics* **15**, 759 (2019).
- [27] S. Changdar, S. Aswartham, A. Bose, Y. Kushnirenko, G. Shipunov, N. Plumb, M. Shi, A. Narayan, B. Büchner, and S. Thirupathiah, *Physical Review B* **101**, 235105 (2020).
- [28] Z. Ni, K. Wang, Y. Zhang, O. Pozo, B. Xu, X. Han, K. Manna, J. Paglione, C. Felser, A. Grushin, *et al.*, *Nature communications* **12**, 154 (2021).
- [29] Z. Ni, B. Xu, M.-Á. Sánchez-Martínez, Y. Zhang, K. Manna, C. Bernhard, J. Venderbos, F. de Juan, C. Felser, A. G. Grushin, *et al.*, *npj Quantum Materials* **5**, 96 (2020).
- [30] C. Le, Y. Zhang, C. Felser, and Y. Sun, *Physical Review B* **102**, 121111 (2020).
- [31] A. Zyuzin and A. Burkov, *Physical Review B* **86**, 115133 (2012).
- [32] D. Son and B. Spivak, *Physical Review B* **88**, 104412 (2013).
- [33] K.-Y. Yang, Y.-M. Lu, and Y. Ran, *Physical Review B* **84**, 075129 (2011).
- [34] G. Sharma, P. Goswami, and S. Tewari, *Physical Review B* **93**, 035116 (2016).
- [35] Q. Chen and G. A. Fiete, *Physical Review B* **93**, 155125 (2016).
- [36] M. Hirschberger, S. Kushwaha, Z. Wang, Q. Gibson, S. Liang, C. A. Belvin, B. A. Bernevig, R. J. Cava, and N. P. Ong, *Nature materials* **15**, 1161 (2016).
- [37] Y. Zhang, Q. Xu, K. Koepnik, J. Gooth, J. v. d. Brink, C. Felser, and Y. Sun, *arXiv preprint arXiv:1805.12049* (2018).
- [38] T. Nag and S. Nandy, *Journal of Physics: Condensed Matter* **33**, 075504 (2020).
- [39] S. J. Watzman, T. M. McCormick, C. Shekhar, S.-C. Wu, Y. Sun, A. Prakash, C. Felser, N. Trivedi, and J. P. Heremans, *Physical Review B* **97**, 161404 (2018).
- [40] S. M. Young and A. M. Rappe, *Physical Review Letters* **109**, 116601 (2012).
- [41] J. Sipe and A. Shkrebtii, *Physical Review B* **61**, 5337 (2000).
- [42] T. Morimoto and N. Nagaosa, *Science advances* **2**, e1501524 (2016).
- [43] M. Yao, K. Manna, Q. Yang, A. Fedorov, V. Voroshnin, B. V. Schwarze, J. Hornung, S. Chattopadhyay, Z. Sun, S. N. Guin, *et al.*, *Nature Communications* **11**, 2033 (2020).
- [44] P. Sessi, F.-R. Fan, F. Küster, K. Manna, N. B. Schröter, J.-R. Ji, S. Stolz, J. A. Krieger, D. Pei, T. K. Kim, *et al.*, *Nature communications* **11**, 3507 (2020).
- [45] Y. Zhang, H. Ishizuka, J. van den Brink, C. Felser, B. Yan, and N. Nagaosa, *Physical Review B* **97**, 241118 (2018).
- [46] L. Wu, S. Patankar, T. Morimoto, N. L. Nair, E. Thewalt, A. Little, J. G. Analytis, J. E. Moore, and J. Orenstein, *Nature Physics* **13**, 350 (2017).
- [47] Q. Ma, S.-Y. Xu, C.-K. Chan, C.-L. Zhang, G. Chang, Y. Lin, W. Xie, T. Palacios, H. Lin, S. Jia, *et al.*, *Nature Physics* **13**, 842 (2017).
- [48] K. Sun, S.-S. Sun, L.-L. Wei, C. Guo, H.-F. Tian, G.-F. Chen, H.-X. Yang, and J.-Q. Li, *Chinese Physics Letters* **34**, 117203 (2017).
- [49] G. B. Osterhoudt, L. K. Diebel, M. J. Gray, X. Yang, J. Stanco, X. Huang, B. Shen, N. Ni, P. J. Moll, Y. Ran, *et al.*, *Nature materials* **18**, 471 (2019).
- [50] S. Lim, C. R. Rajamathi, V. Süß, C. Felser, and A. Kapitulnik, *Physical Review B* **98**, 121301 (2018).
- [51] Z. Ji, G. Liu, Z. Addison, W. Liu, P. Yu, H. Gao, Z. Liu, A. M. Rappe, C. L. Kane, E. J. Mele, *et al.*, *Nature materials* **18**, 955–962 (2019).
- [52] G. Chang, B. J. Wieder, F. Schindler, D. S. Sanchez, I. Belopolski, S.-M. Huang, B. Singh, D. Wu, T.-R. Chang, T. Neupert, *et al.*, *Nature materials* **17**, 978 (2018).
- [53] B. Sadhukhan and T. Nag, *Phys. Rev. B* **103**, 144308 (2021).
- [54] S.-M. Huang, S.-Y. Xu, I. Belopolski, C.-C. Lee, G. Chang, T.-R. Chang, B. Wang, N. Alidoust, G. Bian, M. Neupane, *et al.*, *Proceedings of the National Academy of Sciences* **113**, 1180 (2016).
- [55] B. Singh, G. Chang, T.-R. Chang, S.-M. Huang, C. Su, M.-C. Lin, H. Lin, and A. Bansil, *Scientific reports* **8**,

- 10540 (2018).
- [56] Y. Zhang, T. Holder, H. Ishizuka, F. de Juan, N. Nagaosa, C. Felser, and B. Yan, *Nature communications* **10**, 3783 (2019).
- [57] <https://www.fplo.de>.
- [58] D. T. Son and B. Z. Spivak, *Physical Review B* **88**, 104412 (2013).
- [59] R. Lundgren, P. Laurell, and G. A. Fiete, *Physical Review B* **90**, 165115 (2014).
- [60] W. Kraut and R. von Baltz, *Physical Review B* **19**, 1548 (1979).
- [61] R. von Baltz and W. Kraut, *Physical Review B* **23**, 5590 (1981).
- [62] N. Kristoffel and A. Gulbis, *Zeitschrift für Physik B Condensed Matter* **39**, 143 (1980).
- [63] B. Sadhukhan, Y. Zhang, R. Ray, and J. van den Brink, *Physical Review Materials* **4**, 064602 (2020).
- [64] S. Pal, S. Muthukrishnan, B. Sadhukhan, D. Murali, and P. Murugavel, *Journal of Applied Physics* **129**, 084106 (2021).
- [65] J. Ahn, G.-Y. Guo, and N. Nagaosa, *Phys. Rev. X* **10**, 041041 (2020).